Advanced Characterization Techniques for Weld Microstructures

S. S. Babu, S. A. David and M. K. Miller

Metals and Ceramic Division, Oak Ridge National Laboratory, Oak Ridge, TN 37831

Introduction

Microstructural characterization under in-situ and ex-situ conditions at different length scales is important for understanding phase evolution in welds [1]. In-situ techniques involve observation of weld microstructures using X-ray or neutron diffraction [2, 3, 4] and high-speed photography [5]. Common ex-situ techniques are optical and electron microscopy. Recently orientational imaging microscopy [6, 7] has gained importance due to its ability to correlate crystallographic features with its microstructure.

In addition to traditional microscopy, atom probe field ion microscopy (APFIM) plays an important role in the measurement of compositions at nanoscale. The APFIM has proven to be useful in understanding the role of minor elements on the microstructure evolution [8] and the partitioning between the phases during welding [9, 10, 11]. The current paper describes recent advances in the APFIM, i.e., atom probe tomography that enables nanoscale characterization of material with which one can measure the size, shape and composition of phases in greater detail [12, 13]. The power of this technique in evaluating weld microstructure will be highlighted with three examples.

Atom Probe Tomography

The traditional APFIM instrument combines a field ion microscope and a time-of-flight spectrometer. Field ion microscope images surface atoms of a needle-shaped specimen that is cooled to cryogenic temperatures (20 – 70 K) in an ultrahigh vacuum chamber. After a region of the surface is selected for analysis, the atoms on the surface of the specimen are field ionized by applying voltage pulses. The ions from the surface are repelled from the specimen to the detector through field evaporation. These ions are detected by a single-atom detector. The mass-to-charge ratio of the evaporated ions can be calculated from the time taken to travel the known distance and the applied voltage. This step is repeated and surface atoms are removed in sequence. The concept of extending this method to detect atoms at different location was facilitated by the advance in detector design [13]. This detector allows for measurement of the time-of-flight (identity of ion) and the spatial location of the atom on the surface (X and Y coordinates). The third atom coordinate (Z) along the specimen axis is calculated from the position of the ion in the evaporation sequence. The spatial resolution of the lateral coordinate is limited by small trajectory aberrations of the ion at or close to the specimen surface and is typically ~0.2 nm. The spatial resolution in the depth coordinate ~0.05 nm, is significantly better than the lateral coordinates. This high resolution allows for identification of crystallographic planes in the depth direction.

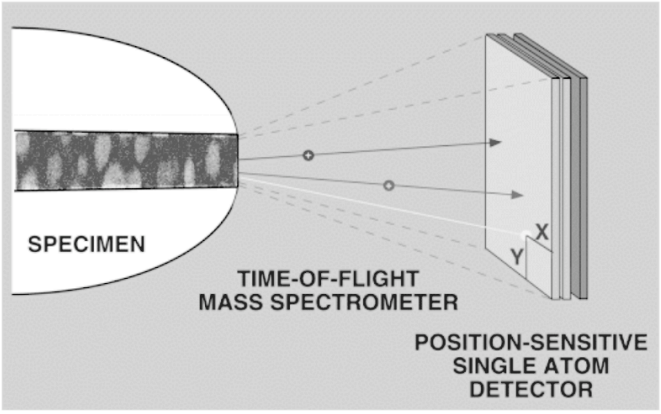

Fig. 1 Schematic illustration of atom probe tomography principle

With the knowledge of X, Y, Z and the chemical identity of atoms, it is possible to reconstruct the material microstructure using computational techniques. The analyzed volume in this technique has typical dimension of 10-20 nm in cross section and up to ~250 nm in length and may contain up to a few million atoms. This new technique, aptly called atom probe tomography (APT) or 3-Dimensional atom probe (3DAP), allows one to evaluate nano scale precipitates, dislocations, clusters, and grain boundary segregation in detail.

The performance parameters of currently available APT or 3DAP instruments are given in Table 1. Further information on the instrument, sample preparation, experimental factors and data analysis are discussed in reference 13. In this paper, the recent results of using APT to characterize weld microstructure are illustrated with three examples.

Table 1 Performance Characteristics for energy-compensated three-dimensional atom probe

Materials	Metals, semiconductors and ceramics with electrical resistivity < 10^{-2} Ωcm
Sensitivity	Single atom
Detection limit	Depends on sample size <100 ppm for large samples
Detection efficiency	60-85% detector/instrument dependent
Spatial resolution (atomic positioning)	Lateral: 0.2 nm Depth: < 0.05 nm
Mass Resolution	m/Δm ~ 500, typical
Mass Range	All elements, uniform sensitivity
Sample size	Up to several million atoms and specimen dependent
Sample area	10-20 nm square, specimen and instrument dependent
Time to perform analysis	Several hours; average ion collection rate 10-30 ions s^{-1}

Nonequilibrium Microstructure in Nickel Base Superalloys:

Past APFIM research on microstructure evolution in nickel base superalloy welds [9, 11] showed that the elemental partitioning characteristics between γ and γ´ phases in slow-cooled welds were similar to that of base metal. However, the partitioning characteristics in rapidly cooled welds were far from equilibrium values and different from that of base metal. These results showed that there is a strong relationship between weld cooling rate and the precipitation of γ´ phase from γ phase. Since weld-cooling conditions are difficult to relate to microstructure evolution due to spatial variation within the weld, there is a need to study the microstructure evolution under controlled cooling conditions. Therefore, the microstructure evolutions in CM247DS alloy under continuous cooling conditions were evaluated [14].

The microstructure of the CM247 sample subjected to water quenching from cooling rates is shown in Fig. 2. The interesting observation in the transmission electron microscopy (TEM) image was that even under rapid cooling conditions imposed by water quenching, the precipitation of γ´ phase could not be suppressed. The rapid cooling led to a large increase in the number density of γ´ precipitates. This result is consistent with the work of Wendt and Haasen [15] who observed the decomposition of γ into two-phase γ-γ´ microstructure in a Ni – 14 at. % Al binary alloy during water quenching. In the water-quenched samples, the shape of the γ´ precipitate was more spherical, in contrast to cuboidal shape in the base metal.

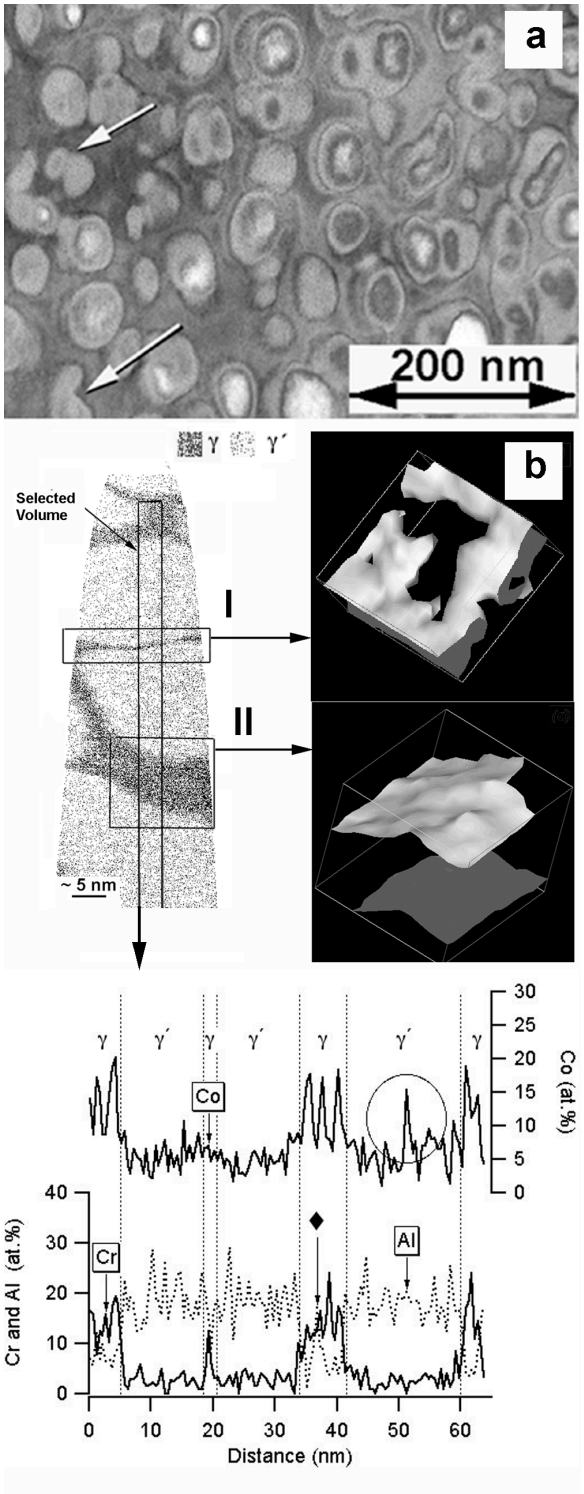

Fig. 2 (*a*) TEM images of water-quenched samples show fine γ´ precipitates and complex morphology (shown by arrows). (*b*) Chromium atom image (left) from APT analysis showing fine γ´-γ morphology, concentration profile (bottom) for the selected volume shown in atom map shows Co enriched region (circled) within γ´ phase and also Al enriched region (marked by a symbol ♦) within the γ phase and iso-concentration surfaces (right) of 15 at. % Cr from regions I and II in the atom map.

The morphology of some of these γ´ precipitates showed some interconnectivity as indicated by arrows in Fig. 2(*a*). However, these images could be artifact due to superimposed images of precipitates at different thickness. Further analyses of water-quenched samples were performed with APT to determine the partitioning characteristics as well as the γ´ morphology. The Cr atom map is shown in Fig. 2(*b*). The atom map shows complex γ´ phase morphology with no regular cuboidal or spherical morphology. Some of the γ´ precipitates had both flat and curved interfaces with the γ phase. The concentration profiles were measured from a selected volume within the data as shown in Fig. 2(*b*).

The morphologies of the γ-phase in two regions "I" and "II" in the Cr-atom map were evaluated [see Fig. 2(*b*)]. The iso-concentration surfaces of Cr at region "I" show that the γ phase is discontinuous along the neighboring γ´ precipitates. This indicates that the γ´ precipitates on either side of the γ phase in "I" are interconnected to each other. This interconnected morphology supports the observations in the TEM. Such interconnection between precipitates is usually expected when the microstructure is in the coarsening stage. During the coarsening stage, the γ´ precipitate may coalesce by interconnecting, which is usually aided by long-range diffusion in both the matrix and the boundaries. However, the mechanism by which this interconnection occurs during rapid cooling conditions remains unknown. In contrast, the γ phase in region II is continuous and the γ´ phase on either side appears to be separate precipitates.

The complex interconnected γ´ morphology in the water-quenched condition could not be rationalized based on nucleation and growth mechanism. It is possible to argue that the observed interconnectivity is due to the impingement of separately nucleated γ´ precipitates. If that is the case, the γ phase region in-between these γ´ precipitates must be enriched in elements such as Cr and Co due to diffusional field overlaps. The concentration of the thin γ phase (~ 20 nm distance from the start) in between the interconnected γ´ precipitates does not show such enrichments (~12 at.% Cr). Based on this observation, it is concluded that the interconnected γ´ morphology is not due to impingement of separately nucleated γ´ precipitates. Therefore, the origin of interconnected γ´ morphology is speculated to be due to nonequilibrium microstructure evolution. Further details on this microstructure evolution can be found in reference 14.

Copper precipitation during neutron irradiation of pressure vessel steel welds

Nuclear reactor pressure vessel steel welds are often embrittled by microstructural degradation during service due to neutron irradiation. Previous research has shown that the submerged arc welds made with copper coated electrode wire leads to embrittlement during service at 200 to 300°C under neutron fluence of 10^{21} to 10^{23} n m^{-2}. Although thermal diffusion is sluggish at this temperature, radiation-enhanced diffusion is expected to increase solute transport and nanoscale features are expected to form [16]. These features are generally under the resolution of conventional analytical electron microscopy and APFIM is an ideal technique to characterize them.

In early 80s, Miller and Brenner characterized neutron irradiated A302B steel plate irradiated for 8 years under a fluence of 2.2 X 10^{23} n m^{-2} and found copper-enriched regions of size less than 10 nm, Mo_2C carbides greater than 10 nm and segregation of Mo, C, V, Cr and Co to ferrite – cementite interfaces [17]. The most common characteristic feature in these neutron irradiated material is the formation of a high-number density of nanoscale (3-4 nm) copper enriched features (11 X 10^{23} m^{-3}) [18]. The copper levels in these features (~1 to 30 at.% Cu) are always below the equilibrium copper levels of the ε copper precipitate. These features are often identified as copper-enriched clusters, zones, precipitates and copper-stabilized microvoids.

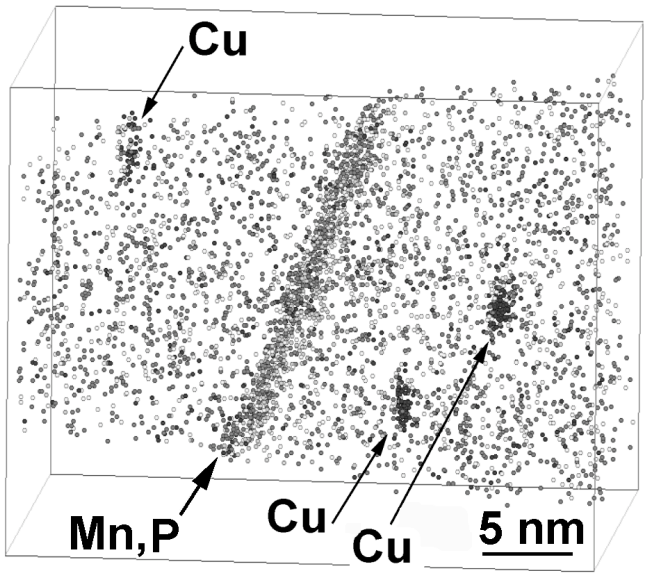

Fig. 3 Atom map of a neutron-irradiated (1 X 10^{23} n m^{-2}) VVER 440 pressure vessel steel weld showing copper enriched regions and a lath boundary with solute segregation

Recent atom probe tomography results from VVER 440 (Ni-Cr-Mo-V steels) pressure-vessel steel weld containing 0.11 at.% Cu is shown in Fig. 3. The atom map of Cu, Mn, Mo and P showed nanoscale copper enriched regions and a ferrite-ferrite lath boundary with P and Mn and small amount of Mo enrichment. The atom map also revealed that the interface of these copper-enriched regions are diffuse and suggest that these features are essentially clusters. Further analysis showed that the Guinier radius of these precipitates is 1.5 nm. Therefore, the result suggests that the copper enriched region have not reached the stage where they have evolved into ε copper precipitates [19]. However, under a neutron fluence of 5.5 X 10^{23} n m^{-2} and a flux of 2.8 X 10^{17} n m^{-2} s^{-1} at 290°C, in a model Fe-1.4at.%Cu alloy, Pareige et al [20] have observed 2-4 nm copper precipitates. These results, show that size and compositional changes of fine nanoscale features can be evaluated by APT.

Grain boundary segregation in Molybdenum Welds:

Molybdenum-based alloys are being considered for neutron flux environments due to their high temperature strength, high thermal conductivity and low thermal expansion. However, their performance is limited by low-ductility (~3 %) in the heat-affected-zone of welds. The lack of ductility in welds has been critical in thick materials with triaxial constraints. It is also well known that controlled addition of substitutional and interstitial elements [21] to the base metal can substantially increase the ductility to 20% even with substantial grain growth. The reason for this improvement in weld performance has been recently studied with atom probe tomography [22].

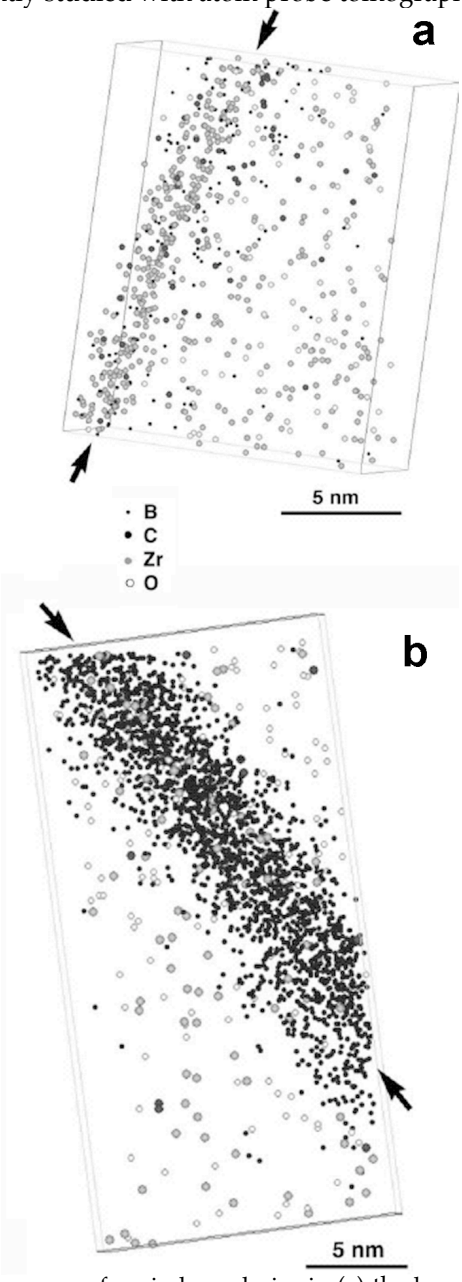

Fig. 4 Atom maps of grain boundaries in (*a*) the base metal and (*b*) the HAZ. The Mo atoms are not shown for clarity. The extensive segregation of B at the grain boundary is evident.

The base material used in this study was prepared by vacuum arc casting method. Minor addition of Zr (.15 wt.%) helps to getter the dissolved O (42 wt.ppm) and N (26 wt.ppm). In addition, 6 wt.ppm of B was added to strengthen the grain boundaries. Field ion microscopy of samples from base metal and heat-affected-zone regions shows some evidence for grain boundary segregation. An atom map of the grain boundary region of the base metal [see Fig. 4(*a*)] shows segregation of Zr, C and B. It is noteworthy that the analysis showed no segregation of O to the interface. The atom map of a grain boundary from HAZ is shown in Fig. 4(*b*). It is evident that the extensive segregation of boron occurs in this boundary.

Detailed analyses of O segregation in both grain boundaries were performed by the Gibbsian interfacial excess method. Interestingly, the Gibbsian excess of O at the grain boundary from the base metal was ($-3.9 \pm 0.6 \times 10^{16}$ atoms m^{-2}) lower than that of heat-affected-zone ($1.1 \pm 0.4 \times 10^{17}$) atoms m^{-2}. This suggests that there is a reduced tendency for O segregation in the base metal compared to that of heat-affected-zone. However, these enrichments in HAZ are smaller than the one reported on pure molybdenum samples earlier [23]. This suggests that the oxygen segregation to the grain boundaries is inhibited due to preferential segregation of Zr, C and B at these boundaries. This change in segregation behavior leads to change in fracture modes from intergranular to transgranular failure.

Summary and Conclusions

The principle of atom probe tomography was introduced. With this technique, one can measure the size, shape and composition of nanoscale microstructural features in materials. The power of this technique was illustrated with three examples.

On rapid cooling from the solutionizing temperature, the γ´ precipitation from γ phase occurs under nonequilibrium conditions. The atom probe tomography revealed interconnected γ´ precipitates as well as nonequilibrium Al enrichment in γ phase and Co enrichment in the γ´ phase.

Neutron irradiation of copper containing pressure vessel steel welds during service in nuclear reactors leads to embrittlement. This embrittlement was related to presence of nanoscale copper enriched regions and segregation of elements to lath boundaries through atom probe tomography.

Addition of Zr, B, C to the molybdenum leads to increased resistance to HAZ cracking. Atom probe tomography showed that Zr, B and C preferentially segregate to grain boundaries, thereby inhibiting oxygen segregation. The reduction of oxygen segregation at grain boundaries leads to better HAZ cracking resistance.

Acknowledgements

Research at the Oak Ridge National Laboratory SHaRE Collaborative Research Center was sponsored by the Division of Materials Sciences and Engineering, U.S. Department of Energy, under contract DE-AC05-00OR22725 with UT-Battelle, LLC. Authors thank Drs. E.

A. Kienik and D. T. Hoelzer of ORNL for helpful comments on the manuscript.

References

1. S. A. David, S. S. Babu, and J. M. Vitek, *Science and Technology of Welding and Joining*, 6, 341-346 (2001)
2. S. S. Babu, J. W. Elmer, S. A. David and M. A. Quintana, *Journal of Proceedings of Royal Society (Mathematical and Physical Sciences) A*, 458, 811-821, (2002)
3. D. Q. Wang, S. S. Babu, E. A. Payzant, P. G. Radaelli and A. C. Hannon, *Metall. Mater. Trans. A.*, 32A, 1551-1552 (2001)
4. J. W. Elmer, J. Wong, and T. Ressler, *Metall. Mater. Trans. A.*, 32, 1175-1187 (2001)
5. A. C. Hall, C. V. Robino, D. O. Maccallum, and M. Reece, MAX-International Convention, Session 2, Paper H, Chicago, March 4-7 (2002)
6. J. N. Dupont, J. R. Michael, and C. V. Robino, *Welding Journal*, 79, 43-48 (2000)
7. T. W. Nelson, J. C. Lippold, and M. J. Mills, *Welding Journal*, 78, 329s-337s (1999)
8. S. S. Babu, S. A. David, J. M. Vitek, and M. K. Miller, *Metall. Mater. Trans. A.*, 27A, 763-774, (1996)
9. M. N. Chandrasekhariah, G. Dubben, and B. H. Kolster, *Welding Journal*, 71, S247-S251 (1992)
10. S. S. Babu, S. A. David and M. K. Miller, *Applied Surface Science*, 94/95, 280-287 (1996)
11. S. S. Babu, S. A. David, J. M. Vitek, and M. K. Miller, *J. de Physique IV*, **6**, C5-253-C5-258 (1996)
12. M. K. Miller and G. D. W. Smith, *Atom Probe Microanalysis*, Materials Research Society, Pittsburgh, PA 15237 (1989)
13. M. K. Miller, *Atom Probe Tomography, - Analysis at the Atomic Level*, Kluwer Academic / Plenum Publishers, New York (2000)
14 . S. S. Babu, M. K. Miller, J. M. Vitek, and S. A. David, *Acta. Mater.*, 49, 4149-4160 (2001)
15. H. Wendt and P. Haasen, *Acta Metall.*, 31, 1649-1659 (1983)
16. M. K. Miller, P. Pareige, and M. G. Burke, *Materials Characterization*, 44, 235-254 (2000)
17. M. K. Miller and S. S. Brenner, *Res Mechan.* 10, 161-168 (1984)
18. P. Pareige, P. Auger, S. Miloudi, J. C. Van Duysen and M. Akamatsu, *Ann. Phys.* C-22, 117-124 (1997)
19. M. K. Miller, *Surface and Interface Analysis*, 31, 593-598 (2001)
20. P. Pareige, P. Auger, and P. Bas, and D. Blavette, *Scripta Metall. Mater*, 33, 1033-1036 (1995)
21. A. J. Byhan, *WRC Bulletin*, 312, ISSN 0043-2326, (1986)
22. M. K. Miller, E. A. Kenik, M. S. Mousa, K. F. Russell, A. J. Bryhan, *Scripta Materialia*, 46, 299-303 (2002)
23. A. R. Waugh and M. J. Southon, *Surface Science*, 68, 79-85 (1977)